Proc. Vth International Workshop, Advances in Signal Processing for Non Destructive Evaluation of Materials
Québec City (Canada),2-4 Aug. 2005. © X. Maldague ed., É. du CAO (2006), ISBN 2-9809199-0-X

Keynote lecture

New approaches to non-destructive evaluation of materials using air-coupled ultrasound

I. Solodov and G. Busse

Institute for Polymer Testing and Polymer Science (IKP) – Department of Non-Destructive Testing, Stuttgart University, Pfaffenwaldring 32, D-70569 Stuttgart, Germany

Abstract

The results of NDE and material characterization with mode conversion of air-coupled ultrasound into plate and surface waves in solids are reported. Single- and both-sided configurations of efficient slanted wave conversion are developed and tested for various materials. An alternative option is based on the excitation of cylindrical plate and surface waves by a focused air-coupled beam incident on a specimen surface. New opportunities of the mode conversion approach are demonstrated in remote mapping of elastic anisotropy, profilometry of thickness, ultrasonic imaging, linear and nonlinear NDE of defects and damage.

Key words: Air-coupled ultrasound, mode conversion, plate waves, surface waves.

1. Introduction

In recent years, air-coupled ultrasound (ACU) has become a routine inspection technique in non-destructive evaluation (NDE) of a wide range of materials and components [1]. However, in conventional ACU-systems, the transmission of ultrasonic energy into solids is extremely inefficient ($\sim 10^{-4}$) due to the mismatch of acoustic impedances (4-5 orders of magnitude for the majority of materials). The situation is aggravated if, in addition, the materials are laminated, porous or highly dissipative. As a result, NDE with ACU is virtually not possible for “inconvenient” materials, like plastics, foams, some composites, wood, and cement based materials.

To increase the elastic coupling between air and solids, one can use the idea of spatial resonance. The first option includes thickness resonance which strongly enhances vibration amplitude (and ACU transmission) in plate-like samples. Focused ACU beams will produce a resonance area confined around a focus spot which can excite efficiently plate waves in a wide angular range. In slanted ACU configurations, the spatial resonance corresponds to constructive interference of the waves along a particular in-plane direction. In thin samples, this causes a resonance generation of plate acoustic waves (PAW) [2] while an efficient excitation of surface acoustic waves (SAW) is expected when the thickness of the specimen is greater than a few wavelengths.

In this paper, the results of NDE applications based on conversion of focused ACU into plate and surface waves are reported. Unlike conventional scanning ACU systems which are used only for defect imaging, the new applications also include remote profilometry of thickness, mapping of in-plane elastic anisotropy, linear and nonlinear NDE of defects and damage with air-coupled plate and surface waves.

2. Material characterization with ACU conversion

2.1. NDE in focused slanted modes of ACU

In a conventional configuration, the ACU produces a localized surface excitation (membrane-type source) which radiates longitudinal waves inside a solid sample. A synchronous vibration of the source at normal incidence of ACU impedes the wave excitation along the surface. The slanted set-

up enables to introduce an adjustable phase variation and to "stretch" the excitation along the surface. Under phase matching conditions, such a distributed source can operate far more efficiently for the in-plane propagating waves, e.g. PAW, SAW or other types of interface waves. For plane waves, the phase matching depends on the ratio between the velocities of sound in air (v_{air}) and the waves generated ($v_{PAW,SAW}$) which determines the resonance angle of incidence: $(\theta_o)_{PAW,SAW} = \arcsin(v_{air} / v_{PAW,SAW})$. However, real transducers radiate ACU with a finite angular spectrum, so that only a part of the incident energy couples to the waves in a solid. To maximise the air/solid coupling in the slanted configurations, the weakly-focusing ACU transducers are proposed which combine an efficient elastic coupling with a high spatial resolution [3].

The efficiency of conversion also depends on the polarization of the waves excited: ACU coupling is provided only to the out-of-plane components of displacement. According to calculations [4], the out-of-plane displacement dominates in the zero-order anti-symmetric modes in thin plates. For this reason, the conversion efficiency into such flexural waves is usually much higher than that for any other plate wave mode. The surface waves are also polarized mainly out-of-plane so that one would expect their strong coupling to ACU.

The experiments used commercial air-coupled equipment including weakly-focused (focus spot 3-4 mm) 400kHz-piezo-ceramic transducers and a standard scanning table (ISEL-PRO-DIN). The experimental arrangements include Focused Slanted Transmission (FST-) and Focused Slanted Reflection (FSR-) configurations shown in *Figure 1, a.* The former comprises a pair of co-axial ACU weakly focused transducers. The flexural waves excited re-radiate acoustic energy from the reverse side to the receiving transducer thus providing maximum ACU transmission through the specimen at $\theta = \theta_0$. The FSR-set-up uses a similar radiation from the front side of the sample and enables a single-sided access for non-contact inspection.

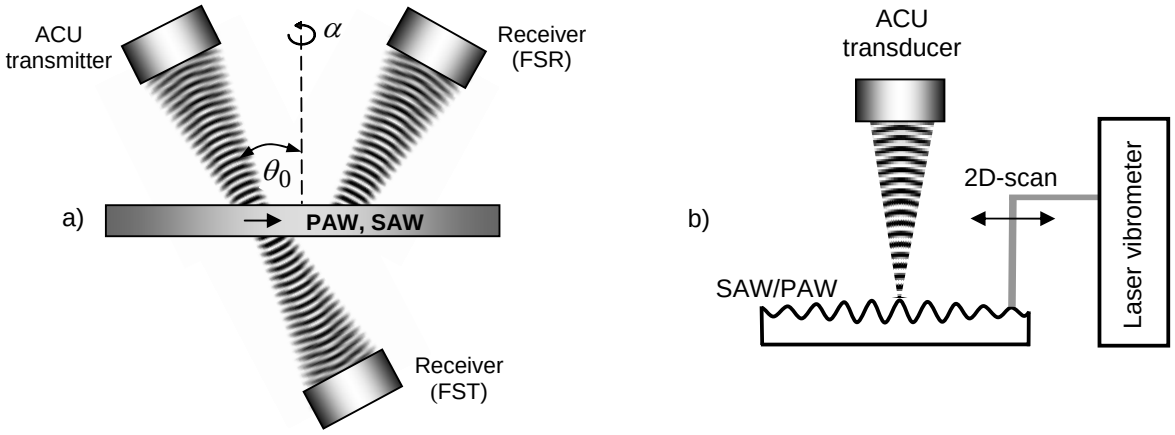

Figure 1. a) - FST- and FSR-configurations; b) – set-up for SAW/PAW wavefront imaging.

2.1.1. Acoustic imaging of defects and profilometry in FS-modes

One of the advantages of using the PAW and SAW for defect imaging is concerned with their strong damping due to scattering by material (and particularly subsurface) inhomogeneities. Besides the increase of acoustic scattering in the defect areas, an additional enhancement of contrast comes from the ACU conversion mechanism: a local variation of θ_0 causes a local drop in the generated (and received) wave amplitudes. The superior amplitude contrast for imaging delaminations in the FS-modes is illustrated in *Figure 2*. It shows ultrasonic scans in normal and slanted transmission of a CFRP laminate (60% fibre content, thickness 4.3 mm) with 4J-low-velocity impact, which induced a 40μm-dent on the front surface as the only visible damage. The damaged

area is well seen in both air-coupled ultrasound scans. However, the FST-image with air-coupled PAW shows a larger area of the induced damage and it also discerns more clearly irregularities in the weave of the carbon fibres in the intact area.

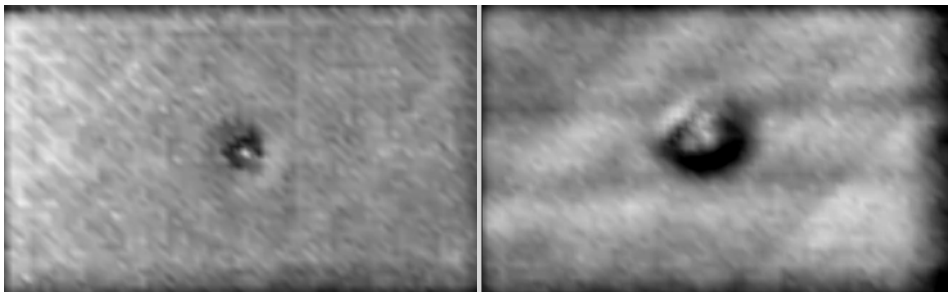

Figure 2. Conventional transmission (left) and FST- (right) scans of impact in CFR-plate (20x15x0.5 cm).

The velocity dependent angular behaviour of the FS-output makes possible a selective conversion of ACU into PAW or SAW which could be applied for NDE of hidden cavities. *Figure 3, c* shows the 2-cm thick Al-sample (30x20 cm) with three cavities of different depths at the bottom side. The thickness of residual material in the cavity areas varies from 1 to 3 mm (*Figure 3).* The results of single-sided scanning (from the intact side) at the resonance angle for ACU excitation of PAW in the 1-mm thick area (*Figure 3, b)* reveal the cavities and enable to distinguish the difference in their depths. The SAW scan exhibits a mirror-inverse contrast with higher output amplitude in parts of regular thickness while the cavities are displayed as low-contrast areas (*Figure 3, a)*.

Since the flexural waves exhibit a strong geometrical dispersion, their velocity depends on the thickness of the specimen. As a result, both the amplitude and the phase of the FST- and FSR-output signals are sensitive to the thickness variation. This property can be used for a remote thickness profilometry of films and coatings using the FS-modes. An example of the FST-B-scanning of inhomogeneous thickness of paint is given in Figure 4. One can see that variation of the delay (phase) of the output signal basically follows the coating profile. The high phase sensitivity of the FST-output to deviation in paint thickness ($\approx 4^0$ / m, Figure 4) confirms a feasibility of high-accuracy profilometry of paint coating on steel substrates typical for automotive industry.

2.1.2. Mapping of in-plane elastic anisotropy in FS-modes

The plane of incidence of ACU in the FS-geometry specifies the direction of wave propagation which can be easily changed by rotating the ACU transducers or the sample (*Figure 1, a*). From measurements of the wave velocity along various directions, the in-plane stiffness anisotropy of a material can be derived. The FS-methodology allows for remote measurements of the in-plane velocity variation by monitoring the changes in the angle of maximum excitation θ_0 or/and phase (φ) of the output air-coupled signal as functions of the azimuth angle α.

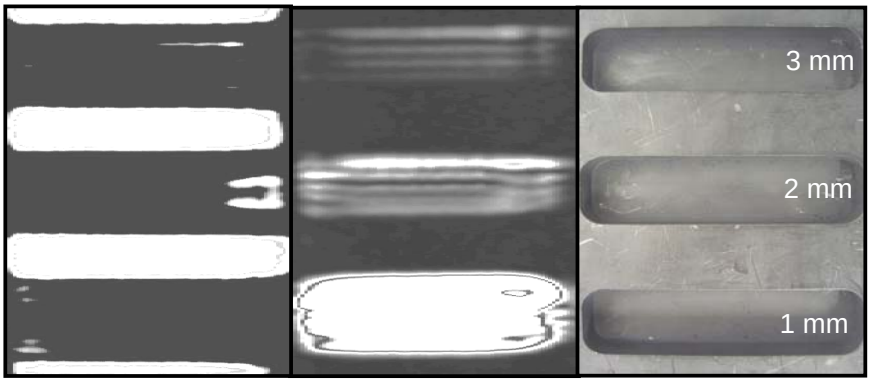

a) b) c)

Figure 3. Single-sided scans of hidden cavities in Al-sample (c) with AC-SAW (a) and AC-PAW (b).

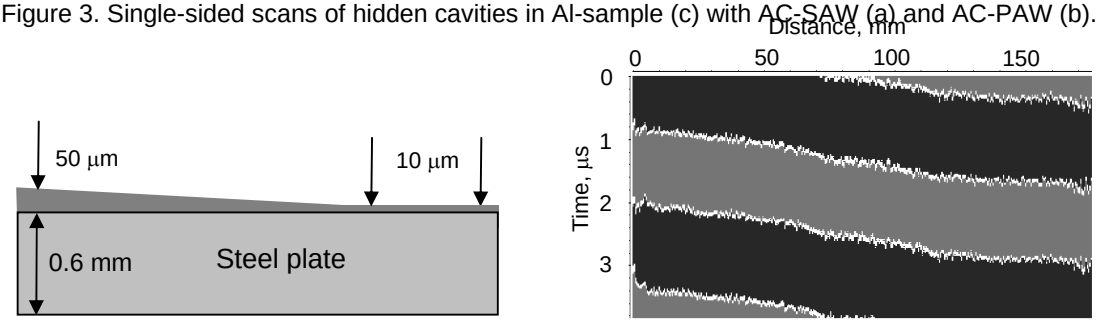

Figure 4. FST-profilometry: (left) configuration of paint coating; (right) FST-B-scan (white lines indicate positions of zero displacements).

Fig. 5 (left) shows the resulting $v_{PAW}(\alpha)$ polar plot obtained by $\theta_0(\alpha)$ measurements for a sample of uniaxial liquid crystal polymer. The "figure-of-eight" symmetry indicates a strong elastic anisotropy: the calculated plate wave velocities range from ≈520 m/s for α = 90° to ≈900 m/s for α = 0 -180° axis which reveals the direction of the highest stiffness. Another example of anisotropy measurements (Fig. 5, right) is concerned with a beech veneer wood laminate which comprises two unidirectional plies of equal thickness (≈ 600 μm) with their L-axis (fibre directions) rotated by 90^0. The cloverleaf velocity pattern confirms the expected 4-fold elastic symmetry in the cross-laminate.

2.2. Waveform imaging mode

An alternative approach to remote measurements of the velocity anisotropy is concerned with air-coupled wavefront imaging. It is based on the PAW and SAW excitation by a surface impact with a focused ACU-beam (*Figure 1, b*). For a point-like source (size of the excitation area smaller than a wavelength), the shape of the generated cylindrical wavefront is independent of the source geometry and is formed by the in-plane stiffness anisotropy of the material. A point-by-point scan of the sample surface using an optical interferometer enables to record and image the wavefront pattern and thus to monitor the material anisotropy. Besides, any defects in the observation area distort the wavefield and hence can also be detected this way [4].

In the wavefront imaging mode, a laser scanning vibrometer was used for detecting cylindrical air-coupled PAW and SAW. The output signal of the vibrometer was compared with the reference voltage to result in recording of the phase synchronized time traces of the vibration velocity for each position of the laser beam. The data acquired over the specimen surface are colour coded and played back as a time sequence of 2D-frames displaying an animated picture of wave propagation.

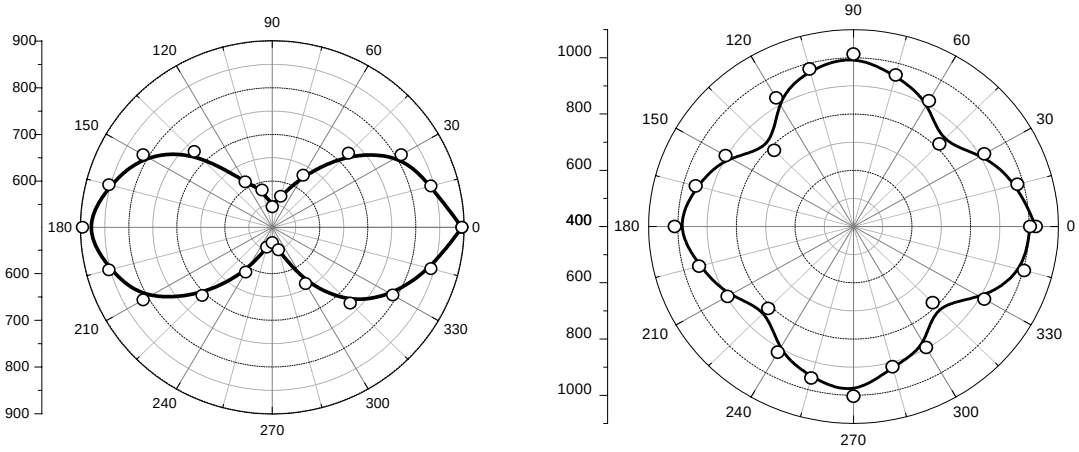

Figure 5. In-plane velocity anisotropy ($v_{PAW}(\alpha)$) measured in FST-mode: uniaxial liquid crystal polymer (left); [0-90^0] cross-ply of beech veneer (right).

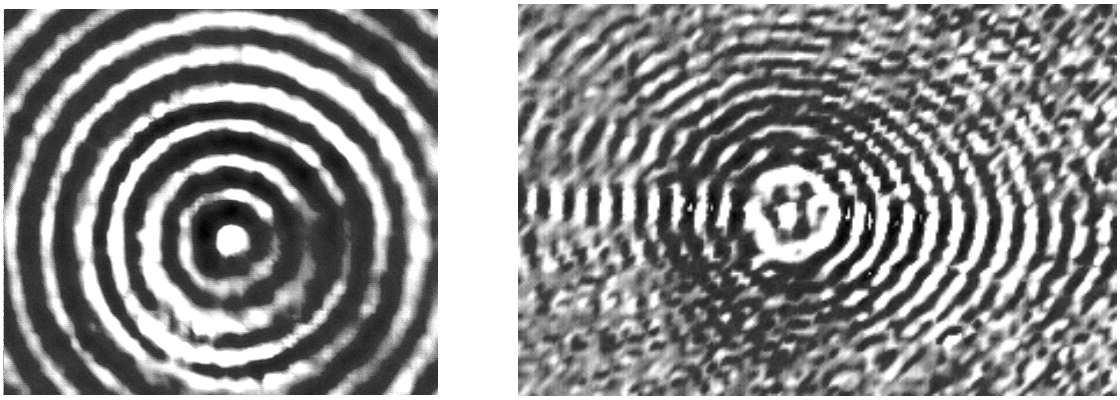

Figure 6. ACU wavefront imaging: SAW in 2-cm thick PMMA sample (left); PAW in a plate of uniaxial liquid crystal polymer (right).

Examples of wavefront imaging are given in *Fig*ure 6. As expected, for isotropic material (PMMA), the SAW wavefronts are close to ideal concentric circles (*Figure 6, left*). On the contrary, the in-plane stiffness anisotropy in a liquid crystal polymer distorts the wavefronts: one can see an evident elongation of the PAW wavefront along the fibre direction (horizontal axis in *Figure 6, right*). This image also demonstrates a high anisotropy of elastic wave dissipation due to a strong scattering in the direction normal to fibres. As a result, the wave energy is focused along the reinforcement direction ("phonon focusing"). Both effects make the wavefront imaging applicable for remote detection of local fibre directions in composite materials.

2.3. Nonlinear NDE with ACU conversion

Another new area of applications of the ACU is nonlinear NDE which is based on measurements of the wave propagation parameters beyond the limit of Hooke`s law. Local material nonlinearity strongly increases in damaged areas and, thus, is a very sensitive indicator of defect formation. A flexible operation of nonlinear NDE can be provided by using the ACU-conversion for non-contact acoustic wave excitation. In addition, the focused nonlinear ACU-option would benefit by probing nonlinearity locally and reading information directly out of the damaged areas.

For acoustic wave propagation in the medium with an ambient strain, the elastic nonlinearity results in a variation of wave velocity with static strain ε [3]:

$$c(\varepsilon) = c_0(1 - \beta_2\varepsilon - \frac{3}{2}\beta_3\varepsilon^2 - ...), \quad (1)$$

where c_0 is the wave velocity in an unstrained body, β_n are the parameters of nonlinearity whose values characterise the presence of defects in a material.

If in tensile tests, $c(\varepsilon)$ is measured locally in the expected fracture area, the damage induced can be revealed by measuring β_n as functions of static strain. Since a major contribution to $c(\varepsilon)$ is from the second-order terms, the parameter to be determined is: $\beta_2 = -(\partial c / \partial \varepsilon)/c_0$. Hence, one has to measure the local acoustic wave velocity as a function of static strain. The value of β_2 defines the rate of stiffness variation: positive values correspond to softening of the material while a negative sign means stiffening. Since the ACU-FST implements a local generation-detection of PAW, it can be applied for NDT of fracture by monitoring $\beta_2(\varepsilon)$ through a loading cycle.

In the experiment, $\beta_2(\varepsilon)$ was investigated for thermoplastic based composites fabricated by injection moulding [3]. The ACU-PAW velocity was derived from measurements of the FST-output phase variation. *Figure 7* shows the results of tensile tests for glass-fibre reinforced polypropylene

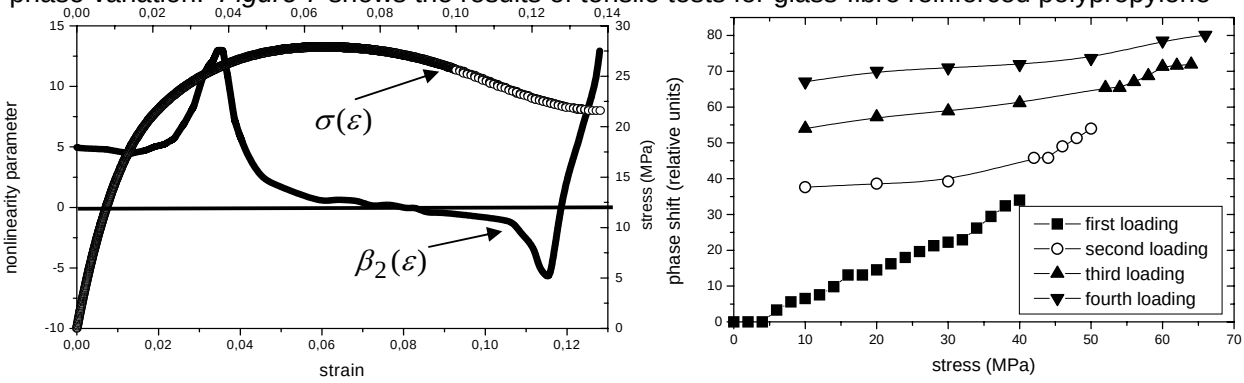

Figure 7. Stress-strain curves and $\beta_2(\varepsilon)$ for tensile loading of 5% GFRP (left); phase shift of FST-output for cyclic loading of glass fibre bundle embedded in a polycarbonate plate.

(5% weight fraction of short glass fibres) and the load applied normal to the fibre directions. In this case, the stress causes a high strain exclusively in the matrix regions between the transversal fibres. As a result, the deformation of the composite, basically, develops similarly to that of the polymer matrix: softening due to molecular untangling (positive β_2) is balanced by their straightening and alignment ($\beta_2 \to 0$). Stiffening of the matrix due to drawing and crazing makes β_2 negative that is a precursor of cracking and eventual quasi-ductile fracture. Further increase in ε, causes a substantial rise in positive β_2 which indicates material damage. Since the β_2 rise precedes the fracture, it can be used as a signal for oncoming failure.

In brittle materials and composites under cyclic loading, one would expect a hysteretic elastic behaviour of material because of crack accumulation with each consecutive cycle. To verify this assumption we measured the phase shift of the FST-output (proportional to PAW velocity) as a function of applied stress for a few loading cycles of glass fibre bundles embedded in a thin polycarbonate plate. Accumulation of irreversible damage is illustrated in *Figure 7, right,* where the measurements of $\Delta\varphi$ in the area of intensive cracking adjacent to the fibre ends are presented. A hysteretic elastic behaviour confirms irreversible damage induced by cyclic mechanical loading.

3. Conclusions

The ACU conversion into plate and surface waves provides new opportunities in remote linear and nonlinear NDE. The focused slanted modes demonstrate superior performance in imaging of defects, enable a high-accuracy profilometry of coatings and mapping of in-plane stiffness anisotropy. The wavefront imaging is applicable for a rapid interrogation of material anisotropy and, in particular, for remote monitoring of uniformity of fibre directions over large areas in composites. Fracture development in tensile and cyclic loading can be traced by using local nonlinear behaviour of air-coupled plate (or surface) wave propagation.

REFERENCES

[1] Rogovsky (A.). - *Development and application of ultrasonic dry-contact and air-contact C-scan systems for non-destructive evaluation of aerospace components.* Material Evaluation, **50**, 1991, p. 1491-1497.

[2] Luukkala (M.), Heikkili (P.), and Surakka (J.). - *Plate wave resonance – a contactless test method*. Ultrasonics, **9**, 1971, p. 201-208.

[3] Solodov (I.), Pfleiderer (K.), Gerhard (H.), Predak (S.), and Busse (G.). - *New opportunities for NDE with air-coupled ultrasound.* NDT&E, (in print, available online 22 August 2005).

[4] Solodov (I.), Pfleiderer (K.), and Busse (G.). - *Laser vibrometry of air-coupled Lamb waves: a novel methodology for non-contact material characterization.* Materialpruefung, **47**, 3, 2005, p. 3-7.

Proc. Vth International Workshop, Advances in Signal Processing for Non Destructive Evaluation of Materials
Québec City (Canada),2-4 Aug. 2005. © X. Maldague ed., É. du CAO (2006), ISBN 2-9809199-0-X

A 2D-FFT signal processing technique to enhance the contrast of air-coupled ultrasonic C-scans

by Antonino M. Siddiolo[1] and Roman Gr. Maev[2]

[1]*Dipartimento di Meccanica, University of Palermo, Viale delle Scienze, 90128 Palermo, Italy;* [2]*Centre for Imaging Research and Advanced Material Characterization, University of Windsor, Ontario, N9B 3P4, Canada*

Abstract

In this work, a Fourier-based algorithm to enhance the contrast of air-coupled ultrasonic C-scans is presented. The performances of the developed algorithm are checked on C-scans recorded in order to monitor the state of conservation of ancient paintings. Experiments on simulated and real ancient paintings have confirmed the ability of the algorithm in recognizing small corrupted regions, replacing them with synthetic values and finally filtering out the high frequency noise. The processed images show an enhanced contrast and an higher signal to noise ratio and appear pretty easy to be interpreted.

Keywords: 2D Fast Fourier Transform, air-coupled C-scans, contrast enhancement.

1. Introduction

In almost all current ultrasonic inspection methods, ultrasonic waves have to be conveyed from a transmitter, into the object to be tested and then to a receiver. This procedure usually requires the use of a good acoustic coupling agent between the transducers and the material to be inspected. Nevertheless, in many applications the presence of a couplant may be undesirable and impractical or simply its use can damage and/or contaminate the investigated object (e.g. aerospace materials such as honeycomb structures, foams, porous and hygroscopic materials, wood and paper based products. On the other hand, if air is chosen as the coupling medium, several problems must be overcome in setting-up a feasible technique [1]. Besides the ultrasound attenuation, which is larger in air than in any other liquid media, the main problem is the acoustical impedance mismatch between air and the most common materials. The amount of transferred energy after each interface is really small and advanced techniques have to be designed to minimize losses at every stage and to achieve an acceptable signal to noise ratio for the inspection. The main techniques are: the use of un-dumped resonant transducers, to maximize the conversion between electric and kinetic energy; the implant of final matching layers, to reduce losses due to the impedance mismatch; the use of low-noise preamplifiers, to minimize any noise pickup on the cables; the optimized electrical design of the receiver circuitry, mainly accomplished by using tunable narrow band filters matched to the toneburst frequency; the use of advanced signal processing techniques, such as the pulse compression technique [2], in order to achieve a good time resolution, even using chirps of longer duration.

In the next section, a description of the air-coupled application will be given, as well as a short presentation of the employed technology and of the adopted procedure; in the same section, the main artifacts of the air-coupled C-scans, which we are dealing with, will be shown. Then, after a brief review of the Fourier theory, the developed algorithm to enhance the quality of the obtained air-coupled C-scans will be described in detail. Finally, some examples of application of the proposed algorithm will be displayed and discussed.

2. Air-coupled application

Before coming deeper to the algorithm, it is useful to give an explanation of the kind of application which we are dealing with. Wooden panel paintings are the object of the present investigation. A wooden

painting can be thought as a layered structure with a support [3]; the last one provides a base for the paint. During its life, the painting is subjected to variations of ambient parameters, like temperature and humidity. In dependence of these daily variations, the different materials that constitute the painting expand and contract themselves of different amounts. In time, the ground (made by several layers of gesso and animal glue) becomes more and more fragile, loosing its former elasticity. Hence, it can not follow the deformations of the wood support any more: cracks appear on the ground and propagate through the painting surface, severely damaging the aesthetics of the art work. Other typical defects that can occur are detachments between layers. If the ground has lost its elasticity, the occurrence of cracks and/or delaminations is unavoidable. The aim of the present research is to develop an air-coupled technique in order to check the state of conservation of paintings [4,5,6].

The ultrasonic pulser/receiver NCA-1000 2E is implemented in the measurement system; the device is based upon the synthesis of an amplitude modulated chirp with a Gaussian profile. Dealing with air transmission and propagation to highly absorbent materials, in order to extend the detection range for a given peak-power and still have an acceptable time resolution, the cross-correlation technique [2] is used. Piezoelectric transducers have been utilized; they represent one of the best solutions to the air-coupled issue and are developed at the Ultran Laboratories [1]. We utilized three couples of transducers, characterized by 200, 500 and 1000 kHz as center frequencies.

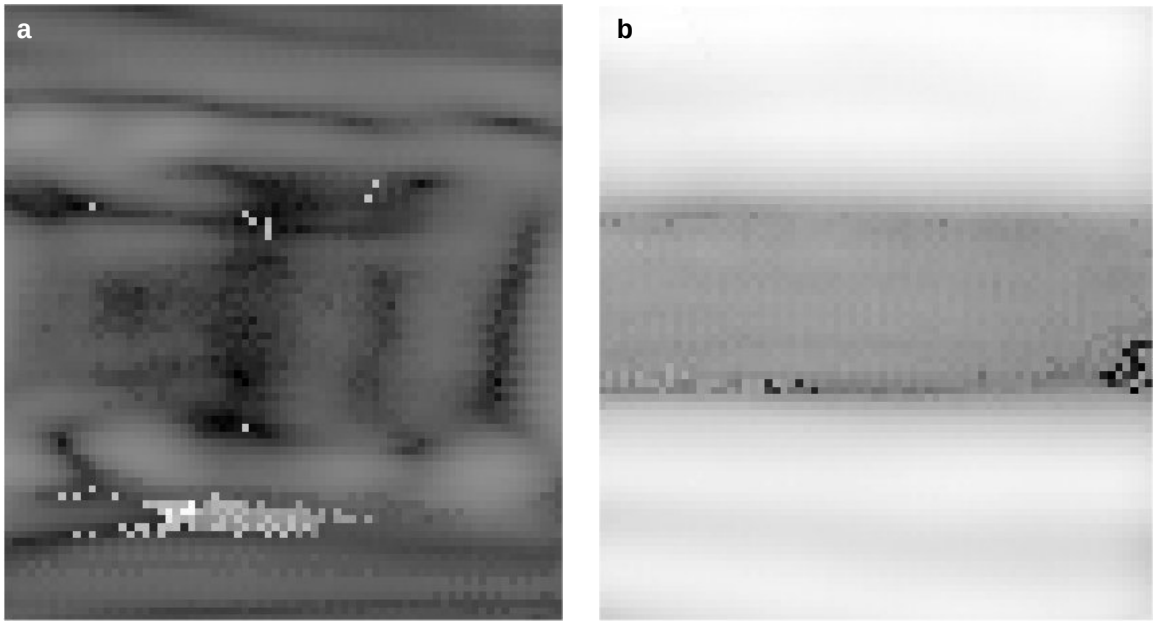

Fig.1.a and b – Original air-coupled C-scans with corrupted regions

Home made models - with simulated defects such as cracks and delaminations - and real paintings were analyzed in single-sided configuration. The transducers were tilted by a proper angle to generate guided waves in the panel and a commercial scanning device was used to control the position of the non-contact transducers. The generated guided waves allowed us to properly detect the presence of a defect in almost all the models tested: the presence of a delamination destroys the correct propagation of the guided wave. The received signal is processed by the system for each position, and data regarding a precise time interval of the compressed pulse are stored. The main information is represented by the Integrated Response, the area underneath the gated time interval. The added benefit of using the cross correlation as the basis for ultrasonic pulse measurements is that, due to the time integration involved, a large signal-to-noise ratio enhancement can be achieved. Nevertheless, the cross correlation procedure leads to instability of the measured parameters of the gated time interval.

For these reasons, C-scans show sometimes regions of incoherent values that affect the quality of the image as a whole, as it is possible to see in the non processed C-scans showed in Fig.1.a and b and related, respectively, to a home-made maple model with a rectangular delamination (a) and a passing horizontal delamination between the wood support and the ground. As it is possible to realize by simply observing the extension of the corrupted regions, it is difficult to cancel the influence of these regions by applying classical filters, such as average or median filtering procedures.

3. Fourier theory and 2D Fast Fourier Transform (2D FFT) based algorithm

A 2D-FFT based algorithm has been developed in order to deal with the above mentioned artifacts. Actually, the used algorithm is a modified version of a previously developed routine designed by the author to properly face missing fringe regions in shadow moiré fringe patterns [7]. Before coming deeper into the core of the algorithm, it is useful a brief introduction regarding the Fourier theory.

A periodic function can be expressed as the sum of sines and/or cosines of different frequency and amplitude (the Fourier series). A function of finite duration (like an image) can be expressed as an integral of sines and/or cosines, multiplied by proper weighted functions (the Fourier transformation). Nowadays, several transformations are coming into use in several applications such as image restoration, coding, pattern description and so on; nevertheless, the Fourier transformation maintains an important role in the image processing. The Fourier transformation of a continuous function f(x,y) of real variables x and y is defined as:

$$\Im[f(x,y)] = F(u,v) = \int_{-\infty}^{+\infty}\int_{-\infty}^{+\infty} f(x,y)\exp[-j2\pi(ux+vy)]dxdy \qquad (1)$$

The u and v variables are thought as frequencies variables; in fact, being $\exp[-j2\pi kx] = \cos(2\pi kx) - j\sin(2\pi kx)$, where $k = u,v$, the F(u,v) function is composed by the sum of infinite sines and cosines. The inverse transformation is definite as follows:

$$\Im^{-1}[F(u,v)] = f(x,y) = \int_{-\infty}^{+\infty}\int_{-\infty}^{+\infty} F(u,v)\exp[j2\pi(ux+vy)]dudv \qquad (2)$$

The Fourier transformation can be seen as a reversible change of coordinates in which the image is represented; during the transformation the information is totally preserved. It is like if in the Fourier space the image is observed from a different point of view. The extension to the discrete case is easy, and one has to speak now about Discrete Fourier Transform (DFT) or Fast Fourier Transform (FFT). The new system of Fourier coordinates in which the image is represented allows one to operate in the Fourier space and manipulate these data, in order to measure particular frequency components in the space domain or to properly modify its values.

The proposed algorithm operates in three steps: during the first step the corrupted regions are located. This operation is accomplished in different ways depending on the artifact nature; each way has a different degree of automation. It is possible: 1) to manually design the mask by simply using Boolean operations, 2) to operate on the histogram function of the image in a manual or totally automatic fashion, or 3) to locally process the image in a semi-automatic way, recognizing which gaps are related to corrupted regions, having previously informed the software on which kind of gray level steps are supposed to belong to corrupted zones and which are not. Actually, the designed mask is not a binary mask, but a labeled mask, which allows us to manage each region of bad values independently by each other ones. The result of the mask creation, regarding the corrupted C-scans previously displayed in Fig.1.a and b, is shown in Fig.2.a and b, respectively.

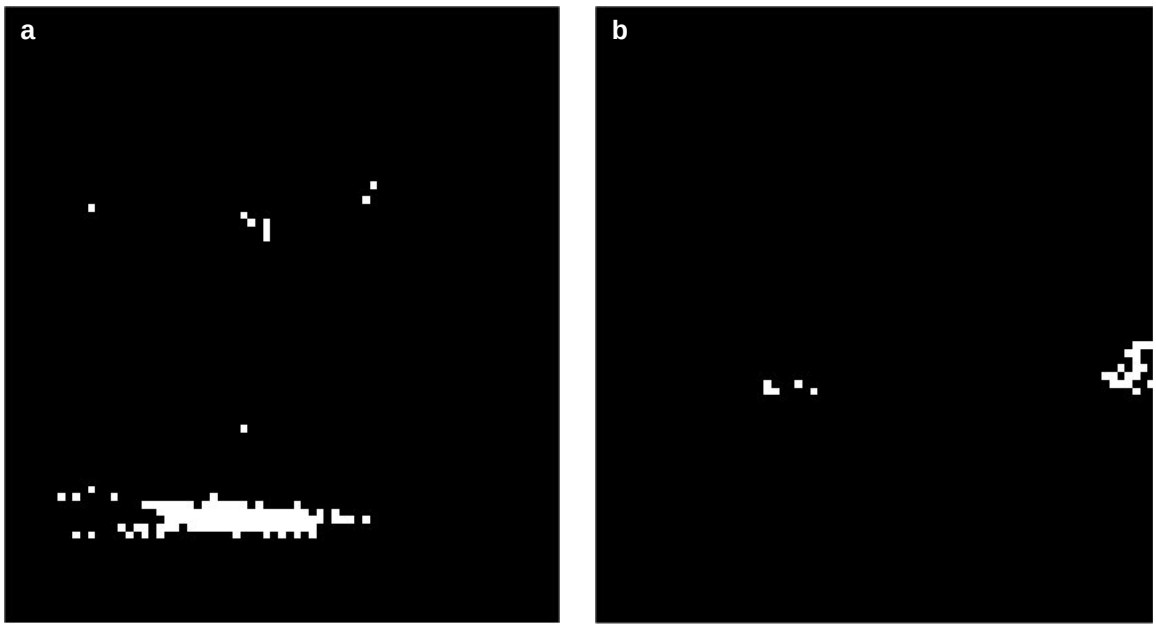

Fig.2.a and b – Created masks to highlight the corrupted regions

After having recognized the artifacts, the next step is represented by the filling operation of the highlighted regions by coherent values; this is performed by properly operating on the spectrum and on the space information. The corrupted values related to each bad region are first replaced by constant values. The proper gray level is calculated by locally processing data on the borders of each zone. At this point, a low-pass filter is designed by using the spectrum of the C-scan so manipulated. The filter is designed by thesholding the image spectrum. The threshold value is calculated by statistical considerations on a region of the spectrum characterized just by noise. Applying the so designed filter on the image, and retaining the information related to the masked data, it is possible to further replace the bad regions with values smoothly varying in passing from the masked to the not masked areas; but the boundary zones are still far from being well connected and joined together. Now, the iterative space-frequency procedure starts. Before performing this operation, a new low-pass filter is designed, by following the criteria above exposed. The image is then iteratively Fourier processed; for each iteration, the following operations are accomplished:

- low-pass filtering of the current image;
- logical application of the mask to the result, in order to locate and isolate the values filling the previously highlighted bad regions;
- image processing of the temporary result. Each region is properly scaled using the information retrieved on its boundaries to accelerate the convergence of the algorithm.
- upgrade of the current image. Using the mask, the current image is upgraded for what concerns the masked regions. In other words, previous values of those regions are substitute with the new ones. These operations will continue until a proper condition is reached, that is - in few words – until the mean variation of the gray level value per pixel, considering the current and the previous image during the algorithm iteration, is lower than a pre-defined value.

The result of the iterative procedure on the C-scans displayed in Fig.1.a and b, on the ground of the created masks that one can see in Fig.2.a and b, is shown in Fig.3.a and b, respectively.

After being restored the continuity of the image, the high frequency noise is removed in the last and third step. This operation is performed by designing - in the way above described - a low-pass filter and applying it on the final result of the iterative procedure now exposed. The final results, regarding the usual C-scans (Fig.1a and b), are shown in Fig.4.a and b.

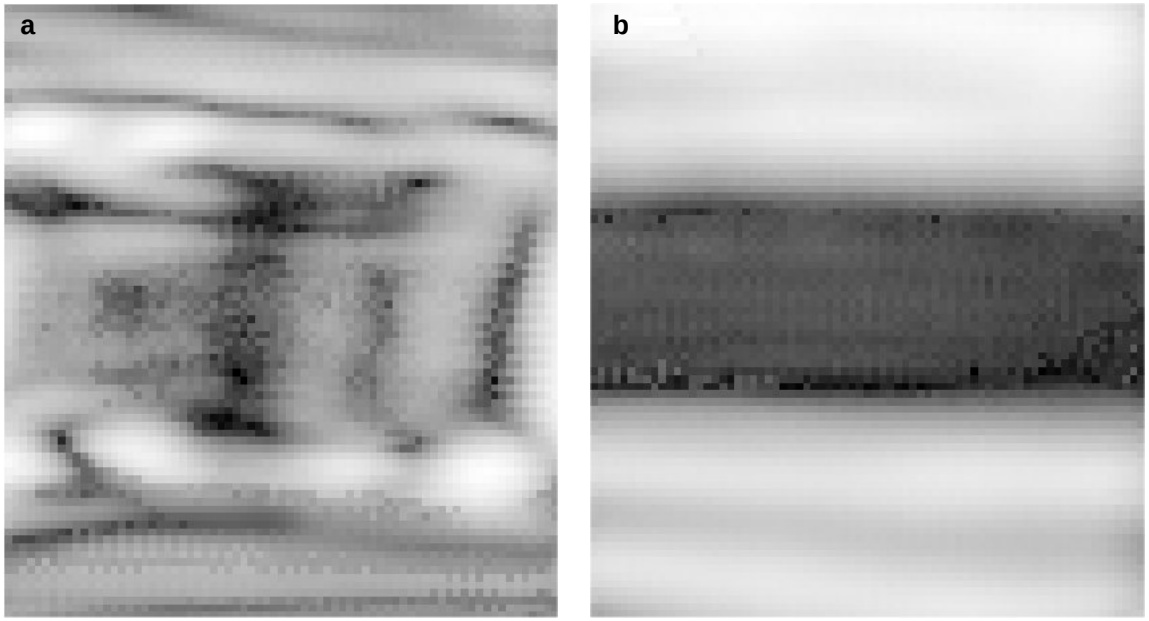

Fig.3.a and b – Result of the space-frequency iterative algorithm to fill the bad regions

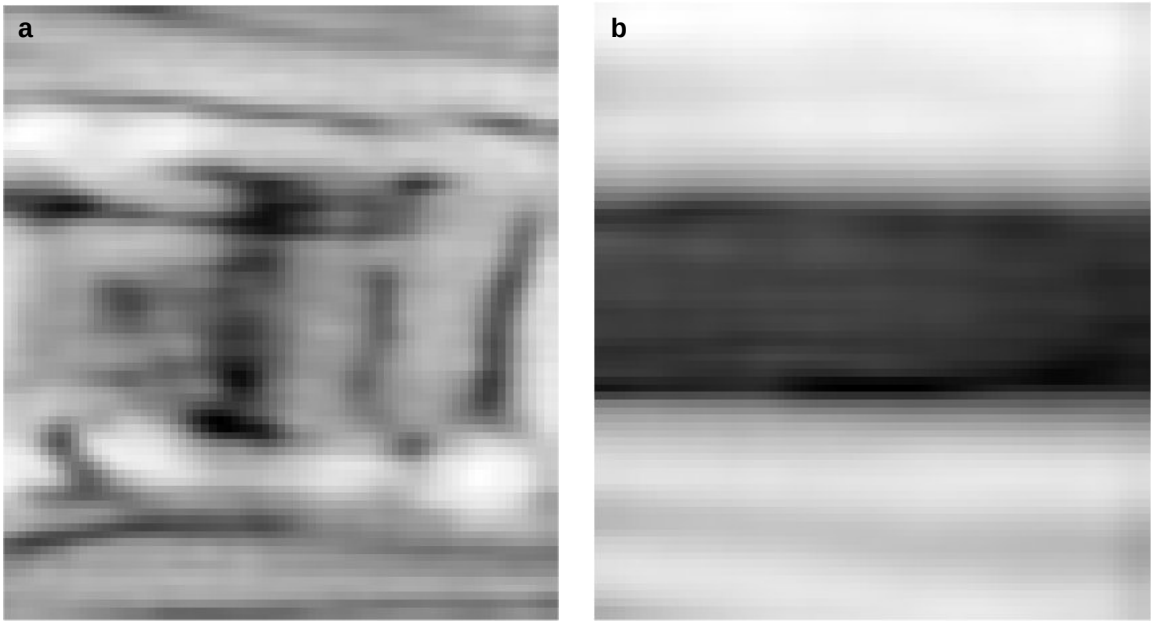

Fig.4.a and b – Final results of the algorithm application

4. Results of the algorithm application and discussion

In the Fig.5, an application of the described algorithm on a real ancient painting is shown. The object of the investigation was a six hundred year old painting coming from a private collection (Fig.5.a - the scanned region is highlighted by a white box). The single-sided C-scan, performed by using the 200 kHz couple of transducers (Fig.5.b), showed various corrupted regions due to the really weak received signal and to the correlation operation involved in the energy measurement. Nevertheless, it was possible to enhance the contrast of the scan by applying the proposed algorithm and the result is displayed in Fig.5.c. The darker regions of the scan represent zones of the interface between the

mahogany support and the ground that are characterized by weak adhesion or incipient delamination. The difference in the received energy between a sound and a defective region was about 30 dBs.

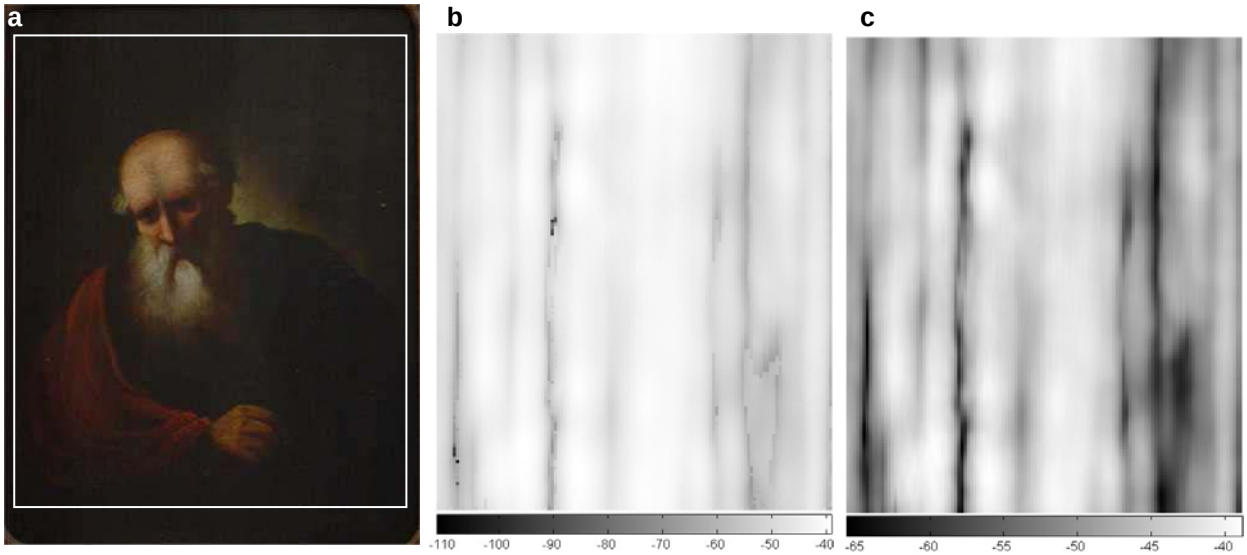

Fig.5.a, b and c. a) Investigated wooden painting, b) original C-scan and c) enhanced C-scan

5. Conclusion

In this work, an algorithm based on the use of the Two Dimensional Fast Fourier Transform has been presented. The aim of the algorithm is to enhance the contrast of ultrasonic air-coupled C-scans. Due to the inherent weak signal received and to the burdensome procedure in processing the information of the received wave packet, these scans present corrupted regions that highly influence the quality of the measurement. The algorithm proposed allows us to detect the presence and the location of these corrupted regions and to profitable fill them with coherent values; this is accomplished by iterative operations in the frequency and space domains, in detail above described. The performances of the algorithm have been proved by means of real and home made wooden panel paintings. The objective of the research was to check the state of conservation of these art works and to localize the presence of defects such as delaminations and cracks between the layers that constitute the structure. Results on real and home made models have been presented; they show that the routine developed is fit and effective to the present application.

REFERCENCES

[1] Bhardwaj M.C. - *Non-Destructive Evaluation: Introduction of Non-Contact Ultrasound,* Encyclopedia of Smart Materials, ed. M. Schwartz, John Wiley & Sons, New York, 690-714, 2002.
[2] Gan T.H., Hutchins D.A., Billson D.R., Schindel D.W. - *The use of broadband acoustic transducers and pulse-compression techniques for air air-coupled ultrasonic imaging*, Ultrasonics 39 181-194, 2001.
[3] Cennino d'Andra Cennini - *Il libro dell'arte (The Craftsman's Handbook)*, 1437.
[4] Murray A. et alii, - *Air-coupled ultrasonic system for detecting delaminations and cracks in paintings on wooden panels*, Nondestructive characterization of materials 6, ed. R. E. Green Jr., New York, 1994
[5] Siddiolo A.M., Maeva A., Maev R. Gr., *Air-coupled imaging method applied to the study and conservation of paintings*, "AI28", San Diego (California, USA), 2005
[6] Siddiolo A. M., Grube O., Maeva A., D'Acquisto L., Maev R. Gr., *Air-coupled acoustical imaging NDE for art object study*, "ART'05", Lecce (Italy), 2005
[7] D'Acquisto L., Siddiolo A.M., *A novel bi-dimensional Fourier transform method to surface measurement by shadow moiré*, "ICEM12", Bari (Italy), 2004

Proc. Vth International Workshop, Advances in Signal Processing for Non Destructive Evaluation of Materials
Québec City (Canada),2-4 Aug. 2005. © X. Maldague ed., É. du CAO (2006), ISBN 2-9809199-0-X

Usability of ECT for Quantitative and Qualitative Characterization of Trickle-Bed Flow Dynamics Experiencing Filtration Conditions

Cristian Tibirna[1], David Edouard[2], André Fortin[1], Faïçal Larachi[2]

[1] *GIREF, Université Laval, Québec, Canada;* [2] *Département de Génie Chimique, Université Laval, Québec, Canada*

Abstract

This work investigates the pros and cons of using the Electrical Capacitance Tomography (ECT) for imaging and quantitative characterization of flow dynamics in a four-phase trickle-bed reactor. ECT use is increasing in non-invasive imaging thanks to its low cost and convenience compared to nuclear ionizing, non-ionizing and other tomography methods. Yet, ECT has low spatial resolution, lack of multi-modality and difficult image reconstruction. The flow dynamics that establish in a four-phase trickle-bed system are complex and prone to instability. This work sets to determine in what measure ECT cat precisely capturing steady-state flow features and unsteady situations: plugging, preferential flowing etc. Many image reconstruction algorithms are tested in the light of the trickle-bed reactor characteristics.

Keywords: electrical capacitance tomography, trickle-bed reactor, multiphase process, image reconstruction, inverse problem.

1. Introduction

The present work is part of a broader project whose main goal is to find ways for increasing the lifetime of catalyst beds in the trickle-bed catalytic reactors used in the hydro-treatment of some oil fractions. The speed at which the catalyst bed is clogging with mineral deposits needs to be reduced. In order to reach this goal, a better understanding of the flow dynamics and clogging physics in trickle-bed reactors is necessary. This requires, among others, to establish a reliable non-intrusive investigation method which can provide better experimental information about flowing and clogging, so that new models can be based on.

Athabasca bitumen contains finely dispersed particles of clay solids, some of which are carried into the gas oil fraction during initial stages of distillation. The distilled fraction has to go to a catalytic hydro-treatment reactor, usually a *trickle-bed reactor*. Suspended particles still present in this fraction are thus a nuisance.

Filtration prior to the reactor bed can remove particles larger than *e.g.*, 25 mm. Fine particles (usually called *fines*) still remain in the fraction. These accumulate in the reactor significantly over many months of operation, by depositing throughout the catalyst bed. This increases the pressure drop to a point where the plant has to be shut down and the catalyst replaced. When this occurs before the end of designed activity life of the catalyst, the operation costs rise unnecessarily.

The interstitial velocity of liquid in the trickle-bed reactor has an important influence on the mechanisms of deposition of fine solids that occurs in the bed of catalyst pellets. The complex mechanisms of the process of fines deposition and pressure drop in the trickle-bed reactor is understood only partially. An effort for finding a good physico-mathematical model for these mechanisms is under way [1]. The validation of this model requires methods of experimental investigation that are both precise and non-intrusive.

Based on previous work focused on three-phase trickle-bed reaction [2], the Electrical Capacitance Tomography (ECT) is pondered in this work as a plausible non-intrusive method of investigation for the deposition mechanisms and flow dynamics in the four-phase trickle-bed reactor. The current investigation focuses on a number of aspects, both favorable and unfavorable, of the ECT as used for non-intrusive imaging of the type of processes mentioned above.

2. Experimental setup

The main elements of the simple experimental setup are schematically represented at *figure 1*. The catalyst bed with a diameter of 57 mm and a height of 920 mm is formed of spherical alumina pellets with a mean diameter of 2.7 mm. The porosity of the catalyst bed was measured at 32%.

A solution of kaolin fines in kerosene, continuously stirred, is sent with controlled flow rates to the top of the packed column. The kaolin was selected because it is the major component of clay minerals found in the Athabasca oil sands. Kerosene was selected due to its similarity – notably given its chemical stability and its low vapor pressure – to the hydrocarbon streams submitted to hydro-treating.

Air and liquid solution are injected through a diffuser for even distribution in the catalyst bed. Liquid flow rate is constant at 0.001 ml/s. The following gas flow rates are used: 0.045 ml/s, 0.123 ml/s, 0.185 ml/s and 0.216 ml/s. A differential pressure sensor measures the pressure drop between the top and the bottom of the packed bed. The tank at the exit of the column allows to store and stir magnetically the output suspension. The inlet concentration of kaolin can be maintained constant by time intervals or varied permanently (see Edouard and Larachi [3]).

The concentration of the kaolin suspension in kerosene is measured periodically in the feed (C_{in}) and in the exit flow (C_{out}) with a Hach 2100P turbidimeter. The maximum concentration was about 1.8 g/l.

For deposition to occur, the suspension of kaolin in kerosene has to be stable. The particle agglomerates should not exceed 10 μm and the use of a surfactant is mandatory. Cetyltrimethylammonium bromide ($C_{19}H_{42}NBr$), also known as CTAB, was added to the kerosene, in proportions of 5% of the mass of kaolin (see [3]).

The ECT equipment used is a PTL300E with a DAM200E sensor controller, from Process Tomography Limited. The sensor has an internal diameter of 63.5 mm, with two adjacent planes of 12 electrodes. The two rows of measurement electrodes are 50 mm high with guard electrodes of 38 mm height placed immediately above and below. The role of the guard electrodes is to confine the electric field measured by the active electrodes to a horizontal section of the reactor. The geometry of sensor's electrodes is given in *figure 2*. The tomograph is controlled from a computer program which also serves for collecting the measurements.

The ECT sensor can be placed at three fixed positions along the column. The top of the sensor is at 330 mm, 580 mm and 860 mm respectively from the bottom of the catalyst bed. The tomographic images obtained at these positions allow to detect differences in the flow dynamics and deposit profiles that might vary with the height of the catalyst bed.

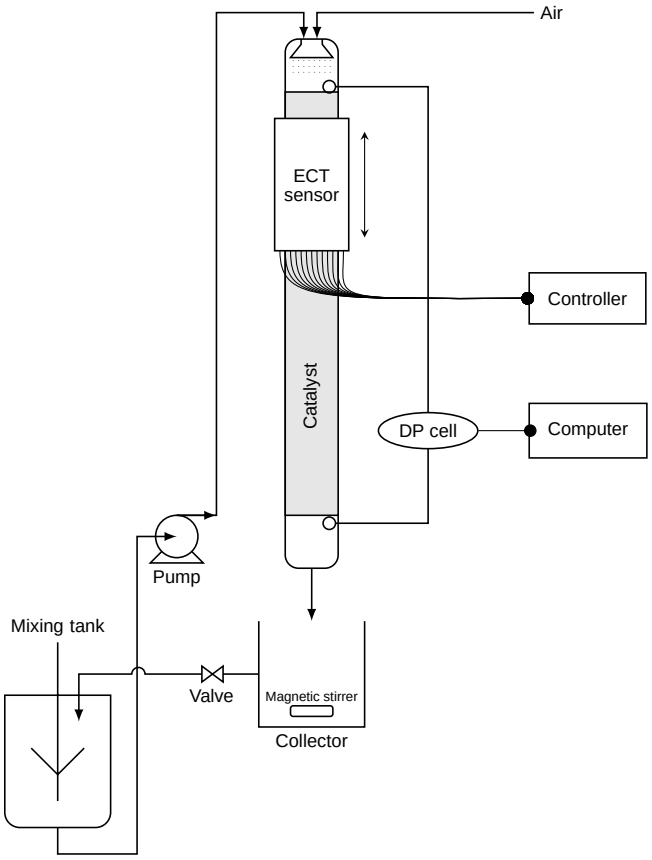

Figure 1: Schematic representation of the experimental setup

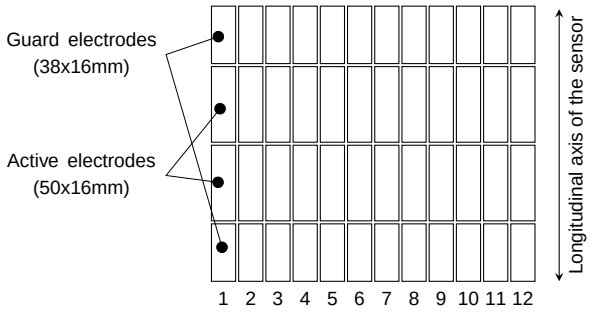

Figure 2: Geometry of the electrodes used in the ECT sensor

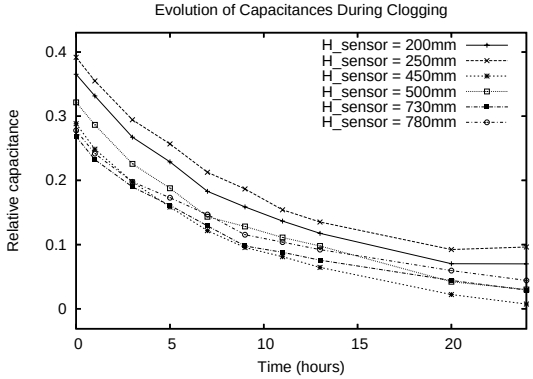

Figure 3: Time variation of the mean relative permittivity in the trickle-bed reactor

3. Advantages and disadvantages of using ECT

ECT is based on dielectric properties of materials (thus well suited for chemical processes) and is non-intrusive (electrodes are placed *on the outside* of the reactor wall)[1]. It is also fast and it is not as expensive as *hard field tomography*[2] while being essentially harmless for human operators and environment. ECT equipment and operation is inexpensive when compared with other non-intrusive tomography methods and this is another major advantage of the technology.

[1] Electrodes can also be placed on the inside of the reactor wall; the essential is that in both configurations, the sensing part of the ECT technology in no way obstructs the hydrodynamics of the sensed system (reactor).

[2] X-ray, γ-ray, nuclear resonance tomographies and so on.

3.1. High speed of ECT allows for detailed characterizations

The current ECT equipment allows for up to 100 tomograms per second to be recorded. The clogging experiment usually goes in about 30 hours from a completely clean catalyst bed to a stable, non-filtering clogging state.

In a first stage, the experiment has been designed to record series of three tomograms, at 330, at 580 and at 860 mm on the height of the catalyst bed (900 mm) once at each 2 hours. This allowed to identify the evolution tendencies of the bed permittivities in the three distinct sections of the reactor (see *figure 3*). Full reactor scans were also performed manually, which allowed to observe liquid and gas flow patterns.

In the next stage of the project, a precise automated ECT scanning mechanism will eventually be put in place, which will allow for full 3D reactor scans to be obtained at given time intervals. This will allow for collecting more detailed data and probably for better differentiation of localized phenomena.

3.2. ECT image reconstruction is a difficult inverse problem

The electric field in ECT is embarrassingly non-linear. This introduces very much indetermination in the reconstruction of the tomograms. The reconstruction itself implies the resolution of an inverse problem of difficult nature, mathematically and numerically.

The fundamental transfer equation which describes the electric field in a plane section of the ECT sensor is a Poisson equation [4]:

$$\nabla \cdot (\varepsilon_0 \varepsilon(x,y) \nabla \phi(x,y)) = 0 \tag{1}$$

where ε_0 is the absolute permittivity of vacuum, ε is the relative permittivity of the material found in the electric field and ϕ is the representation of the electric field. From this equation is deduced the measure of the capacitance between two electrodes [5]:

$$C = -\frac{1}{\Delta V} \iint_{\Gamma} \varepsilon_0 \varepsilon(x,y) \nabla \phi(x,y) d\Gamma \tag{2}$$

After a derivation, linearization and normalization, the best known equation of ECT results:

$$\lambda = Sg \quad \text{or} \quad g = S^{-1}\lambda \tag{3}$$

where λ is the normalized vector of capacitances (of size M), g is the vector of permittivities at each pixel of the zone of measurement (of size N) and S is the sensitivity matrix (of size $M \times N$).

The problem is to determine the unknown g (distribution of permittivities in the system) from the S measured in precise experimental conditions and given a λ measured for the unknown g. This is a badly posed problem because $M \ll N$, hence S is non-invertible.

3.3. Image reconstruction algorithms

Many image reconstruction algorithms are presented in the literature [5, 6] and they are intended for systems containing large features (like gas bubbles) in rapid motion (as in gas fluidization reactors). Very brief descriptions follow.

3.3.1. Non-iterative algorithms

The **Linear Back Projection (LBP)** is the most largely used image reconstruction algorithm for ECT. It is borrowed from the hard field tomography. The fundamental equation of this algorithm is:

$$\hat{g} = \frac{S^T \lambda}{S^T u_\lambda} \tag{4}$$

where u_λ is a unit vector with the same dimension as λ.

The main advantage of LBP is its simplicity, which also makes it fast and easy to perform by a computer. Thus image reconstruction using this algorithm is very fast. The downside consists in the really poor quality of the reconstructed image. An impairing smoothing/smearing occurs in the reconstructed image when compared with the real image.

The **Single Value Decomposition (SVD)** algorithm – and its truncated and filtered versions – is mathematically described as:

$$S = U\Sigma V^T \quad \text{then} \quad \hat{g} = V\Sigma^{-1}U^T\lambda \tag{5}$$

These algorithms offer very interesting image quality for the low computing costs that they imply.

The **Tikhonov regularization** method [7] means:

$$\hat{g} = (S^TS + \mu I)^{-1}S^T\lambda \tag{6}$$

This method seems to be difficult to control and requires arbitrarily chosen parameters (μ).

3.3.2. Iterative algorithms

The **Iterative Tikhonov** method performs, at each iteration, a Tikhonov regularization:

$$\hat{g}_{k+1} = \hat{g}_k - (S^TS + \mu I)^{-1}S^T(S\hat{g}_k - \lambda) \tag{7}$$

The **Landweber and Projected Landweber** methods [8, 9] are iterative algorithms inspired from the research on correcting photographic images.

$$\hat{g}_{k+1} = \hat{g}_k - \alpha S^T(S\hat{g}_k - \lambda) \tag{8}$$

Until very recently, the Landweber algorithm was considered the *"state of the art"* in ECT image reconstruction. Unfortunately it has rather severe numerical inconveniences, related to the necessity of using a number of arbitrary parameters as well as lacking a reliable iteration stop criterium.

The **Simultaneous Iterative Reconstruction Technique (SIRT)** is also inspired from the hard field tomography.

$$\hat{g}_{k+1} = \hat{g}_k - \beta S^T \frac{S\hat{g}_k - \lambda}{\operatorname{diag} SS^T} \tag{9}$$

It is very similar to the Landweber method. Its main advantage resides in the way it is often implemented: β is a weighting vector (allowing to give discriminate importance to specific parts of the measured capacitances vector).

3.3.3. Image reconstruction results

All these classic algorithms were implemented in a programming framework based on the Python programming language and using Python's high performance *Numeric* library. The algorithms were then applied to synthetic images obtained by FEM simulations realized with a special code based on the *MEF*++ library developed by the GIREF research group at Laval University, Québec. A graphical comparison of reconstruction results obtained with these algorithms is given at *figure 4*. The goals of the exercise were:

- to test these algorithms for systems with diffuse features (like diffuse concentration distributions of system components);
- to be able to choose the most convenient algorithm for reconstruction of images from this kind of quasi-static systems;
- to select the better working parameters and iteration stop criteria.

Figure 4 shows how different image reconstruction algorithms behave given a particular original image (phantom). One essential observation is that images of distinct objects (like spots, bars and multiple spots) are relatively well reconstructed; when it comes to annular or quadratic profiles (like those shown in the last three lines in *figure 4*), the reconstructed images don't allow to distinguish essentially different original permittivity setups. The most disturbing is the difficulty to distinguish between annular and parabolic setups. It is almost equally possible for such situations to occur in a plugging trickle-bed reactor and thus the imaging technology we choose should enable us to differentiate them. This could become an important handicap in using ECT for trickle-bed reactors imaging.

3.3.4. Process simulation using *MEF*++

The Finite Element Method library *MEF*++, developed by GIREF at Laval University, was used as a tool-chain for the development of a simulator for the dispersion of the electric field inside a system characterized by a non-homogeneous permittivity distribution. Thanks to the high quality of the MEF++ library, only marginal effort was required for the creation of the simulator code. More notable, special routines were created for the integration of the electric field on surfaces present inside the simulated domain.

More energy was required for the creation of a large number of Finite Element meshes that served as supports for the simulations and for precise image reconstruction. Examples of such meshes are given at *figure 5*. The mixed structured/non-structured grid in *figure 5(b)* is particularly difficult to obtain with the meshing tools available today.

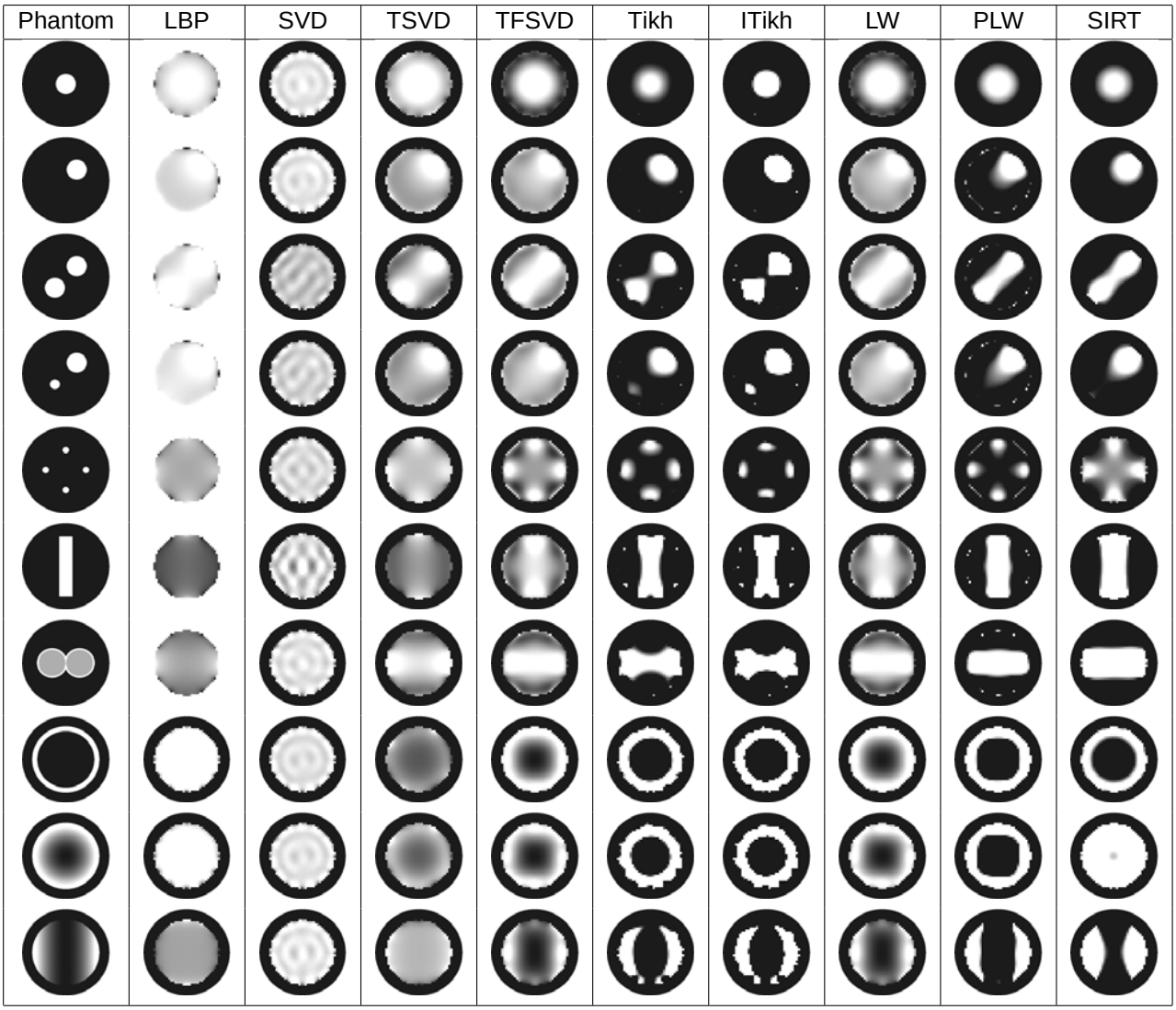

Figure 4: Comparative results of classic image reconstruction algorithms. Algorithms: LBP = Linear Back Projection; (TF)SVD = (Truncated Filtered) Single Value Decomposition; (I)Tikh = (Iterative) Tikhonov; (P)LW = (Projected) Landweber; SIRT = Simultaneous Iterative Reconstruction Technique

3.3.5. Four-phases system

The four-phases trickle-bed reactor used in our setup experiments, for the study of plugging, contains the following phases: solid (catalytic bed of γ-alumina: $\varepsilon_s = 4.5 \times \varepsilon_0$[3]); liquid (kerosene: $\varepsilon_l = 2.2 \times \varepsilon_0$); gas (air: $\varepsilon_g \approx 1.0 \times \varepsilon_0$); suspension of solid fines (kaolin: $\varepsilon_f = 5.0 \times \varepsilon_0$ in kerosene). There is also the surfactant (CTAB: $\varepsilon_f = 36.0 \times \varepsilon_0$). The fines are initially suspended in the liquid phase, but are then depositing on the solid catalyst bed. They are thus forming porous layers in which the pores can be filled either with liquid or with gas. This complex structure puts strains on the detection limits of ECT, as each of these phases has a different relative permittivity contributing to the mean permittivity of the system.

ECT allows for measuring permittivities interpolated linearly between the lowest and the highest values present in the system and fixed by calibration. The literature also presents techniques for imaging objects of three distinct permittivities. Fitting a tomogram to the kind of smooth distribution of permittivities that is seen in trickle-bed reactors requires further refinement of the mathematical models and reconstruction algorithms of ECT.

[3] $\varepsilon_0 = 8.8524 \times 10^{-12}$ F/m is the absolute permittivity of vacuum.

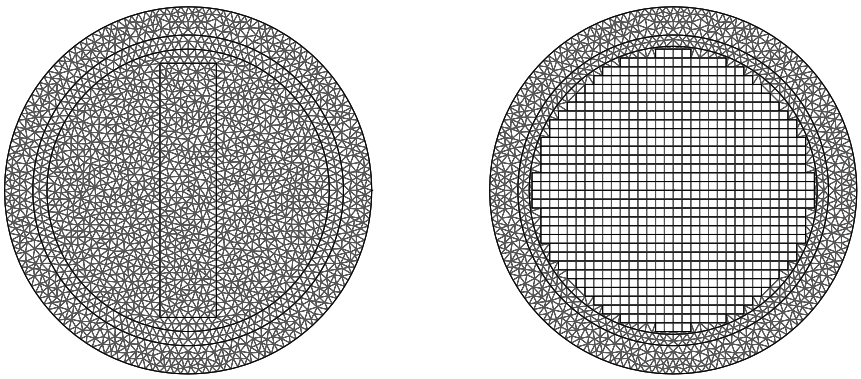

(a) Mesh for simulation (b) Mesh for image reconstruction

Figure 5: Examples of FEM meshes used in ECT

4. Conclusions

ECT is an attractive imaging method to be used for trickle-bed reaction processes. It is fast and inexpensive. It is non-intrusive and this constitutes its main advantage.

The algorithms presented in the literature for ECT image reconstruction are well adapted for detection of objects. Images of smooth composition distributions are difficult to reconstruct. We determined that for this latest kind of images, truncated and filtered SVD (TFSVD) and Landweber methods are the most appropriate. More advanced methods, based on FEM or on neural networks, must be tried.

The technologies involved in ECT are complex and still require improvement and refinement. Work is in course for improving the calibration methodologies and for devising ECT scannings of full reactor length.

In its current state, ECT is applicable to trickle-bed reactor characterizations mostly as a diagnostic technique. Its use for quantitative measurements will become possible after the improvement of reconstruction techniques for smooth permittivity distribution images.

References

[1] Iliuta, I., Larachi, F. and Grandjean, B. *Fines Deposition Dynamics in Gas-Liquid Trickle-Flow Reactors*. AIChE Journal, (49), 2003, pp. 485–495

[2] Reinecke, N. and Mewes, D. *Tomographic imaging of trickle-bed reactors*. Chemical Engineering Science, 51(10), 1996, pp. 2131–2138

[3] Edouard, D. and Larachi, F. *The Role of Gas Phase in Deposition Dynamics of Fine Particles in Trickle-Bed Reactors*. 2005. In preparation

[4] Xie, C., Huang, S., Hoyle, B., Thorn, R., Lenn, C., Snowden, D. and Beck, M. *Electrical capacitance tomography for flow imaging: system model for development of image reconstruction algorithms and design of primary sensors*. Circuits, Devices and Systems, IEE Proceedings G, 139, 1992, pp. 89–98

[5] Yang, W. Q. and Peng, L. *Image reconstruction algorithms for electrical capacitance tomography*. Measurement Science and Technology, 14(1), 2003, p. R1

[6] Øyvind Isaksen. *A review of reconstruction techniques for capacitance tomography*. Meas. Sci. Technol, (7), 1996, pp. 325–337

[7] Tikhonov, A. N. and Arsenin, V. Méthodes de résolution de problèmes mal posés. MIR, Moscou, 1976. Translated from russian

[8] Liang, L. and Xu, Y. *Adaptive Landweber Method to Deblur Images*. IEEE Signal Processing Letters, 10(5), 2003, pp. 129–133

[9] Yang, W. Q., Spink, D. M., York, T. A. and McCann, H. *An image-reconstruction algorithm based on Landweber's iteration method for electrical-capacitance tomography*. Measurement Science and Technology, 10(11), 1999, p. 1065

Proc. Vth International Workshop, Advances in Signal Processing for Non Destructive Evaluation of Materials
Québec City (Canada),2-4 Aug. 2005. © X. Maldague ed., É. du CAO (2006), ISBN 2-9809199-0-X

Detection of subsurface inclusions by magnetic flux density measurements using a fluxgate gradiometer

by Hector Carreon

Instituto de Investigaciones Metalúrgicas, Universidad Michoacana, Edif."U" Ciudad Universitaria, Morelia, Mich. Mexico 58000-888

Abstract

A comparison between published analytical results with measured experimental results of the magnetic field produced by thermoelectric currents of subsurface semi-spherical pure tin inclusions embedded in a copper bar under the influence of an external heating and cooling into the specimen is presented. The experimental magnetic flux density measurements show a reasonable agreement as compared to analytical data with the exception of the intrinsic material background magnetic signal that affected deeply the detectability of subtle imperfections in noncontacting thermoelectric measurements.

Keywords: thermoelectric NDE, magnetic detection, subsurface inclusions

1. Introduction

In general the conventional thermoelectric technique monitoring the thermoelectric power of conductor materials, is sensitive to small changes caused by material imperfections. In order to apply the thermoelectric technique for QNDE material characterization, a conductor with well-defined properties (reference probe) and a known temperature difference along it, is used to evaluate the properties given by changes in the thermoelectric power of a second conductor (test sample). However several effects can affect these changes in the thermoelectric power of the test sample. The most important effects affecting the thermoelectric measurements are those associated with volumetric and contact effects. The volumetric effect is close related to the thermoelectricity phenomena by the kinetics of the diffusion of electrons throughout the material. This effect is mainly affected by chemical composition, anisotropy, hardening, texture etc. The contact effects are related to the imperfect contact between the test sample and the reference probe [1]. On the other hand, the new noncontacting thermoelectric method uses the surrounding intact material as the reference probe; thus provides perfect interface between the region to be tested and the surrounding material. In the self-referencing thermoelectric method the material imperfections naturally form thermocouples in the specimen itself and, in the presence of an externally induced temperature gradient, these thermocouples produce thermoelectric currents around the imperfections that can be detected bias the magnetic flux density B by magnetic sensors from a significant lift-off distance between the tip of the sensor and the material surface imperfection. Even when the material imperfections are rather deep below the surface [2,3]. Figure 1 shows a schematic diagram of the noncontacting thermoelectric measurements process in the presence of material imperfections as most often used in nondestructive materials characterization. In this paper, we review experimental results which demonstrate that the analytical predictions for the case of subsurface semi-spherical inclusions in a homogeneous host material under external thermal excitation truthfully captures the main features of the thermoelectrically generated magnetic field and predicts its magnitude over a wide range of subsurface inclusion sizes embedded in a copper bar and also it shows experimental evidence of the negative effect produced by macrostructural features in thermoelectric NDE especially when the material imperfections (inclusions) are rather deep below the surface. First, we present a review of the analytical model of Reference [4], and then we will proceed by describing the experimental procedure and, finally, discuss the experimental results and compare them to the analytical predictions.

2. Analytical model

In order to illustrate the analytical magnetic field distributions of fully embedded hidden inclusions with the center of a spherical inclusion lies below the surface at a depth *d*, that is deeper than its radius a. We present numerical results obtained by the analytical model described in Ref. [4], in which all spatial coordinates are normalized to the radius of the spherical inclusion as $\boldsymbol{\xi} = \mathbf{x}/a$. The magnetic field is also written in a normalized form as $\mathbf{H} = H_0\,\mathbf{F}(\boldsymbol{\xi})$. Finally, the estimation of the absolute strength of the magnetic field is written as $H_0 = -a\nabla T\,\sigma(S'-S)\Gamma$ where a is the radius of the inclusion, ∇T is the externally induced temperature gradient, σ is the thermal conductivity of the host, $S_{SR} = S' - S$ is the relative thermoelectric power of the inclusion with respect to the host, Γ is a normalized contrast coefficient and $\mathbf{F}(\boldsymbol{\xi})$ is a universal spatial distribution function for all spherical inclusions. Figure 2 shows the two-dimensional distributions of the normal component of the normalized magnetic field for a subsurface spherical inclusion at two different depth distances *d* = *a* and *d* = 2*a* respectively. The magnetic field to be detected rapidly decreases with the depth of the inclusion. The normal component drops from $F_1 \approx 0.4$ at *d* =*a* to as low as $F_1 \approx 0.164$ at *d* =2*a*. The distribution is obviously very similar to that of a surface-breaking inclusion, that was previously published by author *et al*., except that the bipolar lobes are more extended and rounded and accordingly the peak values are slightly reduced. The magnetic field distribution became significantly weaker and wider as the inclusion depth distance increase. The thermoelectric currents flow in opposite directions along two loops on the opposite sides of the inclusion depends on the heat flux direction as predicted by Figure 1.

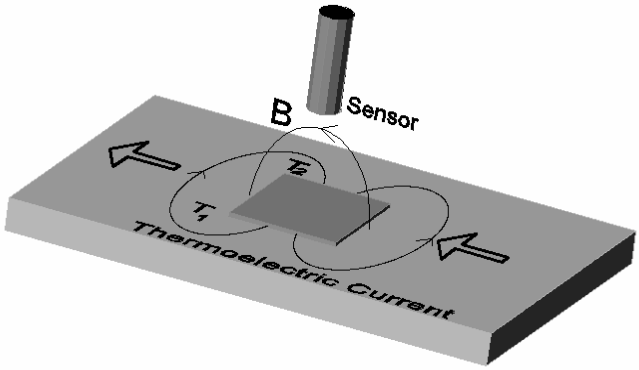

Figure 1 schematic diagram of noncontacting thermoelectric detection of material imperfections by magnetic monitoring of thermoelectric currents.

3. Experimental method

In order to compare the magnitude, over a range of inclusion sizes and lift-off distances, of the analytical magnetic field produced by subsurface semi-spherical inclusions embedded in a homogeneous host material under external thermal excitation with respect to the experimental magnetic field. First, we prepared the specimen, for this reason, it was selected a plate of copper as the host medium and tin as the embedded inclusion. The copper bar (specimen) was cut from a copper plate with a 12.7 mm × 38.1 mm × 500 mm dimensions. The copper specimen was milled to obtain different semispherical holes ranging from 12.7 to 3.18 mm at the specimen surface with a distance of 75 mm between them in order to avoid interference between their individual magnetic fields. The depth of each hole was the same as its radius. Then the specimen was heated to approximately ≈ +300 °C

and filled the holes with molten pure tin in order to obtain surface semi-spherical inclusions embedded in the copper bar. Finally, the specimen was cooled down and milled the surface flat. The 12.7 mm-thick copper bar with the several embedded surface breaking tin inclusions was turned upside down so that the surface-breaking inclusions were at the bottom simulating subsurface semi-spherical inclusions. The copper specimen was mounted and equipped by heater exchangers in order to heat and cool it simultaneously by running water at temperature of $\approx +45°C$ and $\approx +10°C$, respectively. All the assembly was mounted on a translation table for scanning. Since the temperature of the cold and hot water in the laboratory inevitably varied by a couple degrees, the actual temperature difference between the ends of the bar was monitored during the magnetic flux density measurements. The temperature gradient was $\approx 0.7°C/cm$, which is more than sufficient to produce detectable magnetic signals in high-conductivity materials like copper and tin. The magnetic flux density measurements of the different diameter subsurface semi-spherical tin inclusions were detected by a fluxgate (magnetometer) sensor in both temperature gradient directions as shown in Figure 3.

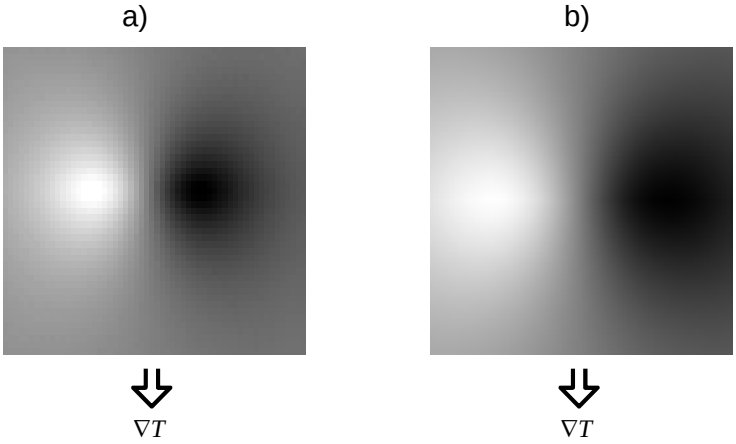

Figure 2 two-dimensional distributions of the normal component of the normalized magnetic field for a subsurface spherical inclusion at two different depths a) $d = a$ and b) $d = 2a$ respectively.

To calculate a quantitative comparison to the analytical predictions, the relevant physical properties of pure copper and tin were taken from standard book references with the exception of the absolute thermoelectric power of tin inclusion at room temperature, which was measured by a Koslow TE-3000 thermoelectric instrument on the largest inclusion itself since it was found to be significantly affected by the sample preparation process (melting and recrystallization) [5]. The specimen was scanned with a 3 axis magnetic field sensor (Mag-03 Bartington) that has a sensitivity of $10\mu T/V$. This fluxgate (magnetometer) sensor has three sensing elements individually potted. The dimension of the sensing element of each sensor (fluxgate) is a cylinder of 15 mm length $\times$ 1 mm radius independently encapsulated with reinforced epoxy with dimensions of $8\times8\times25$ mm. In the experiment, only a pair of fluxgate sensors configurated in a gradiometric arrangement was used to detect the magnetic flux density from the copper specimen. The primary sensor closer to the specimen detects a much stronger signal from the inclusion than the secondary sensor further away, while the two sensors present the same sensitivity for sources at large distances [5]. The geometric center of the fluxgate is approximately 12.5 mm below the tip of the epoxy-encapsulated case, i.e., the $g = 2$ mm apparent lift-off corresponds to a much larger 14.5-mm actual lift-off distance. The baseline distance b and the inclusion depth distance d were chosen to be 28.6 mm and 11.5 mm respectively in our case as shown in Figure 3. The baseline distance and inclusion depth optimization depend on the spatial distribution of the magnetic field to be measured [4,5]. The fluxgate (gradiometer) sensor was located above the centerline of each subsurface inclusion. The magnetic signal produced by the different subsurface tin

inclusion diameters was detected by laterally (normal to the heat flux) scanning the copper specimen at a speed of 20 mm/s.

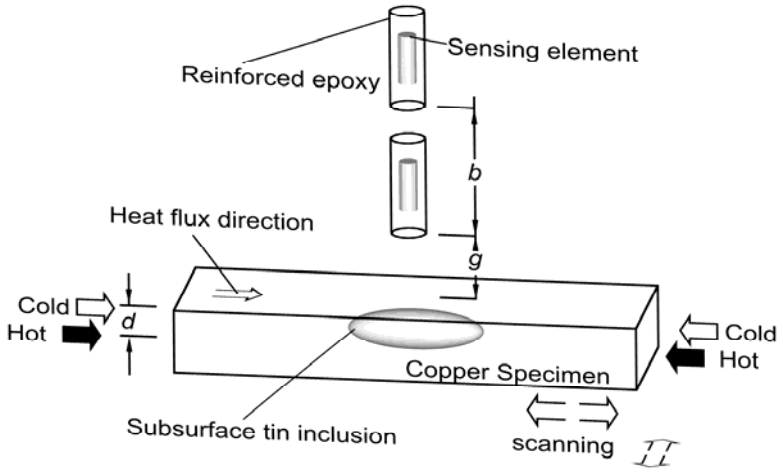

Figure 3 schematic diagram of the experimental set up.

4. Experimental results

Figure 4 shows the magnetic images recorded from two subsurface semi-spherical tin inclusions. These measurements were taken from the copper specimen of 12.7 mm-thick copper bar turned upside down so that the surface-breaking inclusions were at the bottom simulating subsurface inclusions with a depth distance given by *d*. These pictures were taken at 2 mm distance above the copper specimen surface. This apparent lift-off distance is the distance between the tip of the fluxgate magnetometer and the copper specimen surface. However, the sensing element of the fluxgate magnetometer is a 15-mm-long ferromagnetic rod buried at an average distance of 12.5 mm below the surface of the probe, therefore, for the purposes of comparison with the analytical predictions of the magnetic flux density, this experimental configuration corresponds to a much larger 14.5 mm lift-off. The measured magnetic field distributions are very similar in shape to the analytical predictions previously shown in Figure 2. As we expected, the characteristic main bi-polar lobes change sign when the direction of the temperature gradient in the specimen is reversed. These main lobes get wider and the magnitude of the magnetic flux decreases when the lift-off distance is increased. Also the magnetic field became significantly weaker and the spatial distribution of the field revealed some distortions. Beside the previously observed two main lobes, two weaker secondary lobes could also be observed. This particular feature is not predicted by the simple analytical model and is most probably associated with the finite width (12.7 mm) of the copper bar, which is expected to affect the measurements much more when the inclusion is rather deep below the surface due to the fact that the intrinsic material background signature affected the POD of subtle material flaws in the noncontacting thermoelectric technique for QNDE material characterization. Finally, Figure 5 shows how the peak-to-peak magnetic flux density changes with the lift-off distance between 1 and 8 mm for five inclusions of different diameters between 12.7 and 3.18 mm. The solid lines represent the analytical predictions while the solid points represent the experimental results based on the material properties listed. The lift-off distance was corrected for the depth of the sensing element below the surface of the probe and also for the inclusion depth distance, but no other adjustments were made. The results are plotted in Figure 5 that compares the experimentally measured and theoretically predicted magnetic flux densities for different diameters and lift-off distances. Considering the rather crude approximations used in the theoretical model, the large

number of independent material parameters involved in the phenomenon and their inherent uncertainties, and the potential experimental errors associated with the measurements, the agreement between experimental results and analytical predictions over a range of more than two orders of magnitude is so good.

a) 6.35 mm-diameter subsurface semi-spherical inclusion, B ≈ 2.3 nT

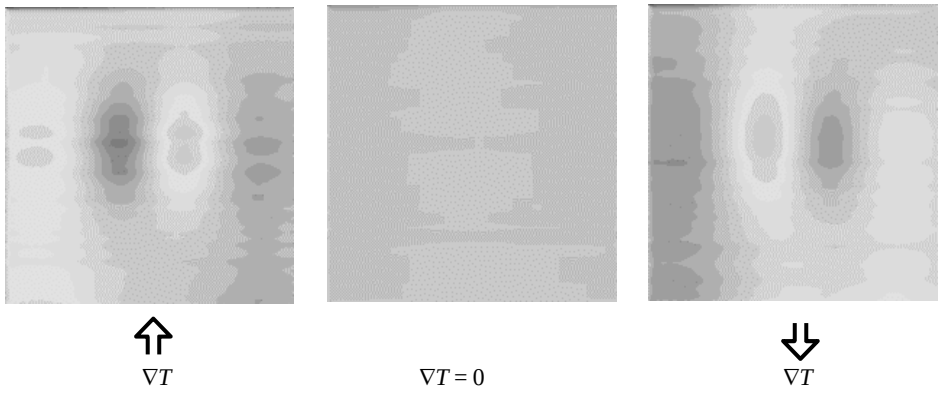

b) 9.53 mm-diameter subsurface semi-spherical inclusion, B ≈ 8.6 nT

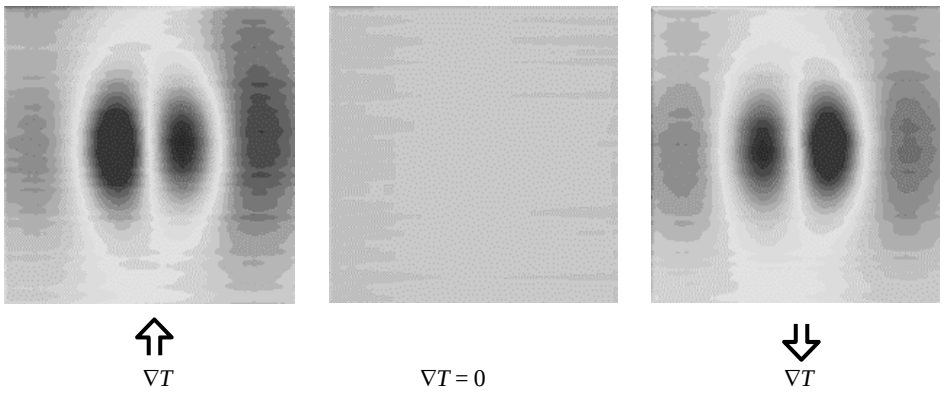

Figure 4 magnetic images of subsurface semi-spherical tin inclusions ($\nabla T \approx 0.7$ ^{O}C/cm, 2 mm lift-off distance, 76.2 mm × 76.2 mm scanning dimension, the peak magnetic flux density B is indicated for comparison).

5. Conclusions

In conclusion, the preliminary measurements clearly demonstrate that the thermoelectric technique for QNDE material characterization is a very powerful one. It should be stressed that it is able to detect inclusions, which are located below the surface. However, this new technique requires a substantial research effort to establish a solid scientific foundation for successful future applications. This goal can be reached by conducting a coordinated theoretical and experimental study of the feasibility of thermoelectric detection and characterization of inclusions and other types of flaws in metals. The results also indicate that the detection sensitivity of the noncontacting thermoelectric method can be limited by unwanted background signal that interferes with, and often conceals, the inclusion signals to be detected. The main sources of such adverse background signals in thermoelectric NDE are the intrinsic variations of the material properties of the specimen to be inspected.

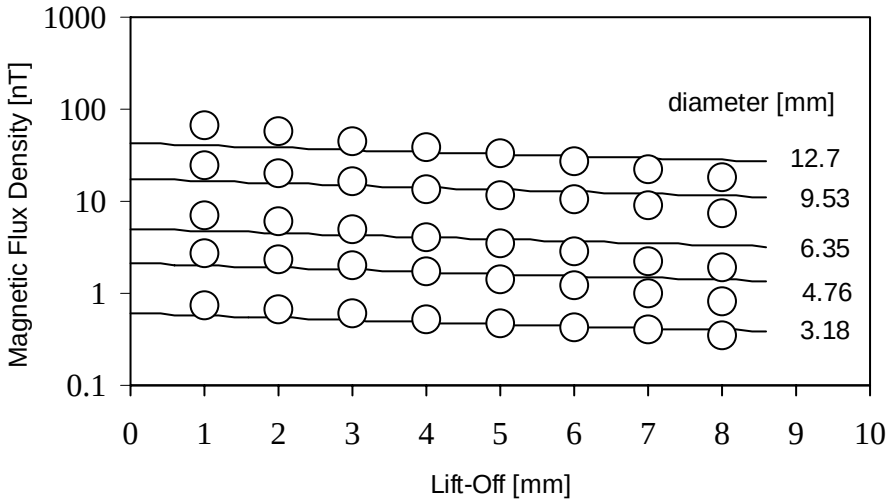

Figure 5 comparison between the experimentally measured and theoretically predicted peak-to-peak magnetic flux densities plotted as functions of the lift-off distance for subsurface semi-spherical tin inclusions in copper.

REFERENCES

[1]FULTON (J.), WINCHESKI (B.), and NAMKUNG (M.).- *Automed weld characterization using the thermoelectric method*, Nondestructive Evaluation Science Branch, NASA 1993; Langley Research Center.

[2]TAVRIN (Y.), KRIVOY (G.), HINKEN (J.) and KALLMEYER (J.).- *A thermoelectric method to detect weak local structural changes and inclusions in metal part.* in Review of Progress in QNDE, Vol. 20. AIP, 2001. p. 1710-1716.

[3]. CARREON (H.), LAKSHMINARAYAN (B.) and NAGY (P.*).- Thermoelectric background signature due to the presence of material property gradients.* in Review of Progress in QNDE, Vol. 23. AIP, 2004. p. 445-452

[4] NAGY (P.) and NAYFEH (A.).- *On the thermoelectric magnetic field of spherical and cylindrical inclusions.* Journal of Applied Physics Vol. 87, 2000, p. 7481-7490.

[5] CARREON (H.), NAGY (P.) and NAYFEH (A.).- *Thermoelectric detection of spherical tin inclusions in copper by magnetic sensing.* Journal of Applied Physics Vol. 88, 2000, p. 6495-6500.

[6] NAYFEH (A.), CARREON (H.) and NAGY (P.).- *Role of anisotropy in noncontacting thermoelectric materials characterization.* Journal of Applied Physics Vol. 91, 2002, p.225-231.